Experimental analysis and simulation of the melt pool behaviour in laser powder bed fusion of pure tungsten

Alfred Sidambe[1*], *Peter* Fox[1] and *Kate* Black[1]

[1]Department of Materials, Design and Manufacturing Engineering, School of Engineering, University of Liverpool, Brownlow Hill, Liverpool, L69 3GH, United Kingdom

Abstract. The processing parameters used in additive manufacturing directly affect the final properties of the product. This study has used single-track formations to study how parameters affect localised regions of molten tungsten when selectively melting pure tungsten powder. A sequence of individual track experiments was performed and the results compared to numerical simulations using OpenFOAM™. Tungsten melt tracks were produced using laser focus offsets of 0 and 1 mm, corresponding to beam diameters of 50 and 43 µm at the surface, respectively. The beam diameter is defined by the radial distance from the centre of the beam where the intensity has dropped to 0.135 of peak intensity. 200W laser power was used during experiments and simulation. The laser was scanned at 50, 138, 225, 313 and 400 mm/s, resulting in different melt formations. The laser energy densities correlated with the experimental melt widths ranging from 89 to 208 µm and with simulated melt volume fractions ranging from 0.39 and 0.79. Comparisons of the experimental and simulation results yielded correlation coefficients (R^2) values ranging from 0.958 to 0.988. The numerical model was assessed and its suitability for tungsten laser melting discussed.

1 Introduction

A growing number of industries are adopting additive manufacturing (AM) to reduce production costs of expensive, intricately designed components which are produced in limited quantities. One commonly used AM technique is the laser powder bed fusion (LPBF) process, where a high-powered laser selectively fuses metal powder into solid parts based on data from slicings of a 3-dimensional Computer-Aided Design file, building the structure in successive layers. The size of each layer usually ranges from 30 to 50 µm [1, 2]. The interest in processing refractory metals such as tungsten (W) using LPBF has steadily increased over the last few years. However, processing tungsten with LPBF is challenging compared to other metals such as stainless steel because of tungsten's exceptionally elevated melting point, a transition from ductile to brittle temperature (DBTT) range of 200 to 400°C which makes

* Corresponding author: a.sidambe@liverpool.ac.uk

tungsten crack easily as a result of residual stresses, and a high thermal conductivity of 175 W/m/K which affects thermal transfer [3, 4].

To address this issue, there have been a various numerical models established in studies to investigate thermal behaviour during LPBF of tungsten with the aim of understanding the heat transfer mechanisms that can affect the melting and cooling of tungsten [5, 6]. To further close the research gap, we have carried out research which develops the results of our previous work [7] by carrying out numerical analysis and calculating the volume fraction of the molten fluid tungsten during LPBF using the Open-Source Field Operation and Manipulation (OpenFOAM) software. We have analysed the behaviour of the melting of tungsten as well as its solidification in respect to the LPBF processing parameters. Our study has investigated the molten pool configurations and variations in behaviour using slow and fast scan laser speeds as well as differing laser beam diameters.

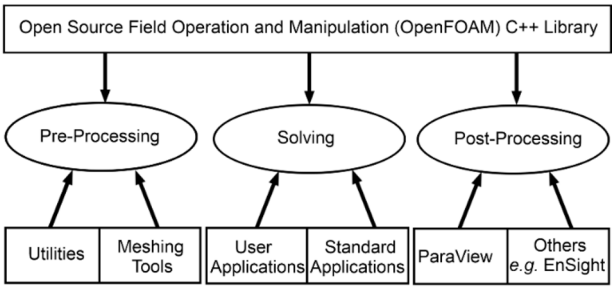

Fig. 1. Overview of OpenFOAM structure [8].

Fig. 1 shows the overview of the OpenFOAM structure. In OpenFOAM, the *icoReactingMultiphaseInterFoam* solver which handles the interaction of multiple phases involved in LPBF was selected for use. It solves the continuity and momentum equations for two fluids, applying the Volume of Fluid (VOF) method to capture phase-fraction dynamics. This solver addresses fluid flow, turbulence, heat transfer, laser heat sources, and phase changes such as melting, solidification and evaporation. It is especially well-suited for simulating laser-based processes, welding, and additive manufacturing techniques like LPBF [9].

In addition, the *icoReactingMultiphaseInterFoam* solver facilitates mass and heat transfer between phases and supports optional bi-directional radiation interaction through the Discrete Transfer Radiation Model (DTRM), including the capability to model reflection at the interface of the phases. The DTRM enables simulation of collimated radiation flux (laser source). However, in this work, the simulations of the laser were introduced into OpenFOAM via an imported convection boundary condition with accompanying Gaussian distributed laser beam [10] which we found to be more compatible with the study.

1.1 Modelling governing equations

OpenFOAM works by splitting the physical domain into small cells to calculate flow of the fluid, governed by the continuity equation (Equation 1) and the transient Navier-Stokes equation (Equation 2). The temperature field is calculated using the pressure p, density ρ, identity tensor $\underline{I}$, time t, volume force vector $\underline{F}$, dynamic viscosity μ and the fluid flow velocity vector $\underline{u}$. For simplicity, the equations are reduced to represent incompressible laminar flow, incorporating the temperature T, heat capacity at constant pressure Cp and thermal conductivity. ∇ represents the divergence operator which helps to determine whether a fluid is compressing or expanding at a given point.

The continuity equation ensures mass conservation and is given by [9]:

$$\frac{\partial \rho}{\partial t} + \nabla \cdot (\rho \underline{u}) = 0 \qquad (1)$$

and the time dependent Navier–Stokes equation can be expressed as:

$$\frac{\partial (\rho \underline{u})}{\partial t} + \nabla (\rho \underline{u} \otimes \underline{u}) = \nabla \left\{ -p \cdot \underline{I} + \mu \left[\nabla \underline{u} + (\nabla \underline{u})^T \right] \right\} + \underline{F} \qquad (2)$$

and the field of the temperature is determined by the equation of the temperature:

$$\rho C_p \left(\frac{\partial (T)}{\partial t} + \underline{u \cdot \nabla T} \right) = \nabla \cdot (\kappa \nabla) \qquad (3)$$

In the *icoReactingMultiphaseInterFoam* solver, these equations are used to simulate the behaviour of multiphase flows with phase change. The solver calculates the volume fraction α_i of each phase i within a mesh cell. In this study we have tracked the liquid phase volume fraction (αLiquid) using the VOF method, which involves solving a transport equation for the phase fraction.

2 Experimental methods

2.1 Laser powder bed fusion

2.1.1 Laser beam profiling

The selective melting of pure tungsten powder was performed using a Renishaw AM125 machine, which is equipped with an ytterbium fibre laser that has an output power of 200W. Experiments which focused on optimising the laser focus offset to maximise the irradiance were carried out. Investigations also centred on whether an optimised laser spot size could minimise the heat affected zone (HAZ), as managing the HAZ is known to reduce microcracking [11].

Experiments were performed to melt tungsten powder prior and post-optimising the profile of the TEM_{00} mode laser beam. The optimisation process utilised a beam profiler, model Spiricon SP620, supplied by Ophir Photonics (Jerusalem, Israel). As illustrated in Fig. 2, the optimal focus offset (f) was identified as 1 mm, resulting in a laser beam whose diameter (ϕ) was 43 µm at surface being irradiated. The beam diameter is defined by the radial distance from the centre of the beam where the intensity has dropped to 0.135 of peak intensity. At a focus offset of 0 mm, the beam diameter increased to 50 µm, as shown in Fig. 2 (b). The TEM_{00} mode laser beam power density distribution and beam diameter at 200 W during profiling are presented in Fig. 2 (c). According to Equation 4, which defines the TEM_{00} mode laser beam power distribution in the xy-plane, the reduction in beam diameter to 43 µm led to a maximum intensity that is 25% higher.

$$(x, y) = \frac{8P}{\pi d^2} exp\left[- \left(\left(\frac{2\sqrt{2}}{d} \right)^2 . (x^2 + y^2) \right) \right] \qquad (4)$$

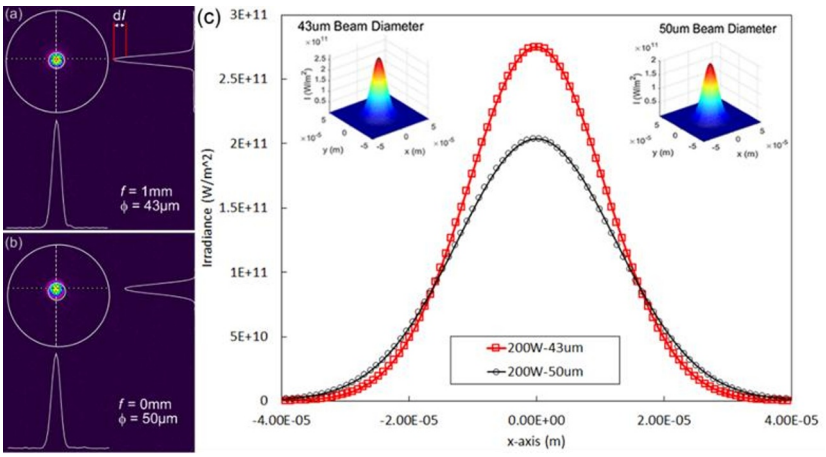

Fig. 2. The optimised focal shift (a) f=1 mm, ϕ=43 μm (b) f=0 mm, ϕ=50 μm. dI illustrates the difference in the resultant irradiance. Simulated irradiance distributions and beam diameters obtained as a result of the profiling of laser (c).

2.1.2 Single track melting of tungsten

The study utilised tungsten powder that is both highly pure and highly spherical, produced through Plasma-Spheroidisation and supplied by Tekna Plasma Systems Inc. (Quebec, Canada). Fig. 3 (a) illustrates the particle size distribution and shows that the powder exhibits a unimodal distribution, with a predominant particle size around 45 μm. The sharp increase in the cumulative volume curve indicates a narrow size distribution, which is advantageous for LPBF. Fig. 3 (b) presents a scanning electron micrograph (SEM) which qualitatively depicts the highly spherical morphology, good surface texture and uniformity of the powder. Table 1 presents the chemical composition of the powder, highlighting its low oxygen content (0.009 wt. %) and high purity (99.1 wt. % tungsten).

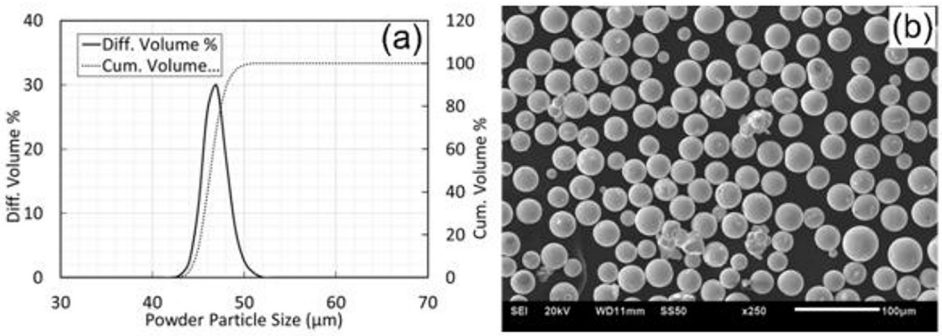

Fig. 3. (a) Powder particle distribution for tungsten and (b) powder morphology.

Table 1: Elemental composition of the tungsten powder utilised in LPBF processing.

Tungsten Powder Composition (weight %)						
W	O	Ti	Mo	Al	Ta	Residual
>99.1	0.009	0.001	0.003	0.001	0.003	<0.001

The experiments were carried out using argon as the shielding gas and with 200 ppm of oxygen remaining to eradicate impure elements. The studies involved single-pass melting of lines using a laser power of 200W and laser scan speeds of 50, 138, 225, 313 and 400 mm/s, resulting in 2D laser energies ranging from 10 to 93 J/mm², prior and post-optimising the profile of the TEM_{00} mode laser beam. The melt tracks were produced on tungsten substrates that had undergone grit blasting and polishing. The 2D linear energy input was computed from the combined effects of laser power, scanning velocity, and diameter of beam, as shown in Equation 5 [12].

$$\mathcal{E}_{2D} = P_{Laser}/(\nu_{scan} \cdot \emptyset_{spot}) \quad (5)$$

The two-dimensional linear laser energy density $\mathcal{E}_{2D}$ is defined as a function of laser power P_{laser}, scan speed v_{scan}, and laser beam diameter ϕ_{spot}. This parameter was chosen for use in this study because it is a parameter which varies with both the speed and diameter of the laser beam, offering a more representative measure of the effective energy input during processing. Melt track widths were characterised via light optical microscopy (LOM) and quantitatively analysed using ImageJ software. Melt pool morphologies were examined using a JEOL 6610 (Akishima, Japan) scanning electron microscope (SEM) operated at 10 kV, as well as a Zeiss Gemini 450 SEM equipped with an electron backscatter diffraction (EBSD) detector.

2.2 Numerical modelling

2.2.1 Heat source and laser beam model

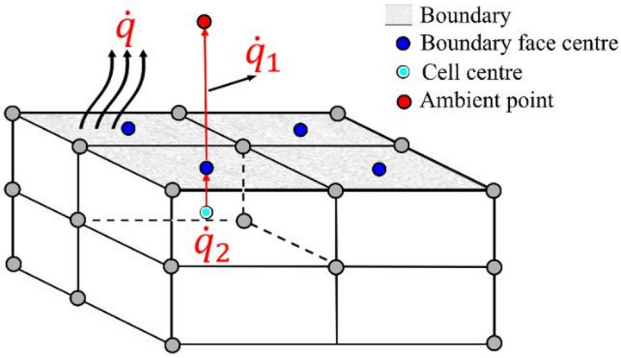

Fig. 4. Conversion of a convective boundary condition into a discrete mesh within the proposed computational domain.

In this work, the simulations of the laser were introduced into OpenFOAM via an imported convection boundary condition (*laserConvectionBC*) with accompanying Gaussian distributed laser beam. The boundary condition was downloaded, compiled and added on to the *icoReactingMultiphaseInterFoam solver* as a free-standing library and compiled with the *wmake* command. To enable this functionality within the simulation, the library was activated by including the line libs ("liblaserConvectionBC.so") in the *controlDict* file. This allowed the customised boundary condition to be written directly into the temperature field configuration [13]. To model surface cooling, convective boundary conditions were applied in place of the standard conductive boundary conditions. These convective conditions were formulated based on the difference in the temperature between the surface and the ambient

environment. The resulting heat flux is directed from the hotter region to the cooler one, ensuring realistic thermal behaviour during the simulation as shown in Fig. 4

In this approach, the relationship governing heat transfer at the interface is given by:

$$h \cdot (T_{Face} - T_{Amb}) = \kappa \cdot \frac{T_{Cell} - T_{Face}}{\delta} \quad (6)$$

Here h denotes the thermal coefficient for convection, T_{Face} represents temperature at boundary face centre (blue point in the image) and T_{Amb} is the ambient temperature at an ambient point (red point). This equation ensures that the heat flux on the material side (right-hand side of the equation) equals the flux on the ambient side of the boundary (left-hand side). The temperature T is measured in kelvin (K), δ represents the distance between the cell centre and the face centre, κ denotes the thermal conductivity and the heat flux $\dot{q}$ is given in watts per square meter (W/m²). Thus, the term $\kappa \cdot \frac{T_{Cell} - T_{Face}}{\delta}$ represents the heat transfer due to conduction within the material from the cell centre to the boundary face. According to the principle of energy conservation, the heat fluxes on both sides of the boundary interface must be equal. This is expressed as:

$$\dot{q}_1 = \dot{q}_2 \quad (7)$$

In this context, the dot over q signifies a vector component in the surface normal direction. Hence, the heat transfer occurring outside the material surface is defined by:

$$-\dot{q}_1 = h \cdot (T_{Face} - T_{Amb}) \quad (8)$$

Within the material, the internal heat transfer is described using the temperature gradient normal to the surface, leading to:

$$-\dot{q}_2 = K \cdot \frac{\partial T}{\partial n} = K \cdot \frac{T_{Cell} - T_{Face}}{\delta} \quad (9)$$

These equations together form a consistent model for heat exchange across the boundary during laser processing, maintaining continuity and energy balance between the material and its surroundings. In this study the ambient point was positioned close to the boundary face.

2.2.2 OpenFOAM simulations

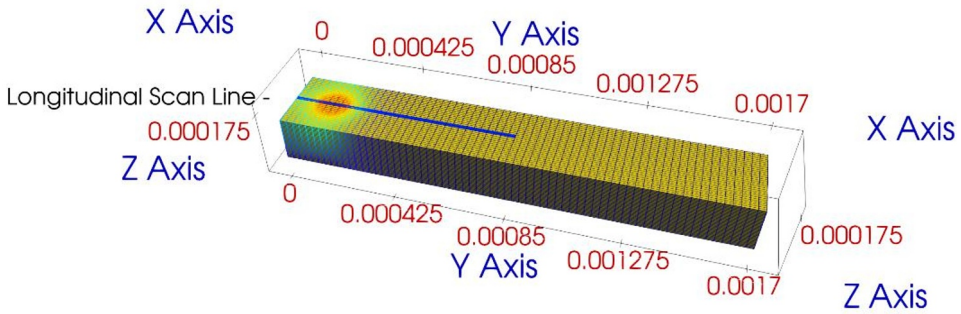

Fig. 5. Model dimensions and mesh, a computational domain considered for the single-layer LPBF simulation in OpenFOAM.

Simulations in OpenFOAM (version 1912) used a substrate and domain with dimensions: x=280 µm, y=1700 µm, z=175 µm (Fig. 5). The selected domain size avoids boundary condition uncertainties in the heat affected zone (HAZ). A simple mesh was created using *blockMesh,* a utility used for generating structured hexahedral meshes. The laser travelled along the longitudinal scan line as shown in blue in Fig. 5 and stopped before 850µm. Results were processed and visualised using ParaView 5.8.0 software. Results of the thermal and melt volume fraction evolution were obtained using thermophysical properties and property parameters of tungsten as shown in Table 2.

Table 2. Thermophysical and phase property parameters for both solid and liquid tungsten as used in the simulations [3] [17] [18].

Property	Designation	Value	Unit
Solid temperature	*T*	Below 3695	K
Density	*Rho*	19600	kg/m^3
Density of liquid	*Rho0*	17600	kg/m^3
Atomic mass	*molWeight*	183.84	g/mol
Specific heat capacity of solid	*Cp*	134	J/kg·K
Specific heat capacity of liquid	*Cp*	300	J/kg·K
Thermal conductivity of solid	*kappa*	174	W/m·K
Dynamic viscosity	*mu*	4.0×10^{-3}	Pa·s
Coefficient of thermal expansion	*alpha*	4.5×10^{-6}	1/K
Enthalpy change of evaporation	*Hf*	1.92^{5}	J/kg
Enthalpy change of fusion (solid)	*Hf*	0	J/kg
Heat transfer coefficient (heating)	*HTCheating*	37197	W/m^2·K
Heat transfer coefficient (cooling)	*HTCquenching*	600	W/m^2·K
Prandtl number	*Pr*	1.7	
Interface Model Constant	*Cu*	1^{9}	
Mass Transfer Model Constant	*C*	1^{6}	
Activation Temperature	*Tactivate*	3650	K

In Table 2, the high melting point (3695 K) indicates that the processing requires substantial energy input, and this necessitates precise control of laser parameters to achieve effective melting without excessive vaporisation. The high density (*Rho*) is expected to influence energy absorption and molten pool dynamics, while the thermal conductivity leads to efficient heat dissipation, thereby mitigating thermal gradients and minimising residual stresses brought about by the high melting point. The specific heat values from Table 2 indicate the energy required for temperature changes in tungsten, which is expected to positively impact laser power and scanning speed settings [19].

3 Results

3.1 Experimental melt pool morphologies

The melt track formations and widths of the tungsten powder subjected to LPBF were closely related to the 2D linear laser energy density, which includes laser beam diameter and laser scan speed, as shown in Equation 5. Fig. 6 displays optical micrographs of ten tungsten single melt tracks on the substrate obtained using the different scan parameters. Details of notation can be found in Table 3. Low scan speeds, which can be said to have contributed to low melt viscosity of molten tungsten promoted sufficient melt spreading, leading to large melt pools. The results were further analysed for melt pool depth penetration using SEM' techniques. Fig. 7 shows the results of the sections of the 50 mm/s scans (a) 43 µm beam diameter and (b) 50 µm beam diameter. The micrographs of the non-etched cross sections did not reveal a

clear boundary between melt pool and substrate. Instead, a seamless transition between substrate microstructure and solidification structure exhibited epitaxial growth in the microstructure. The focus offset optimisation increased the melt pool height as shown in Fig. 7 (W_50_43). This is also expected for the penetration depth. The keyhole and conduction mode characteristics of the melt pool which are widely discussed in AM were not observed in the instance.

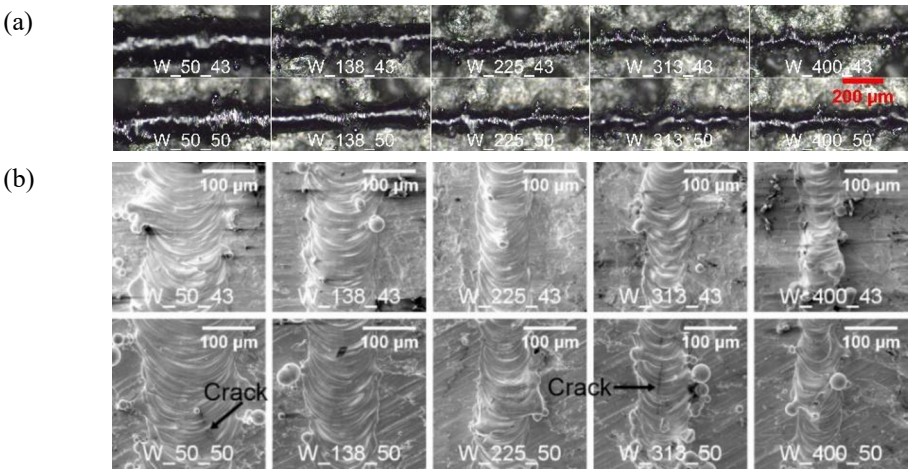

Fig. 6. (a) Optical micrographs show continuous W single melt track morphologies on grit blasted substrates (b) SEM's show the morphologies of the W single melt tracks on polished substrate.

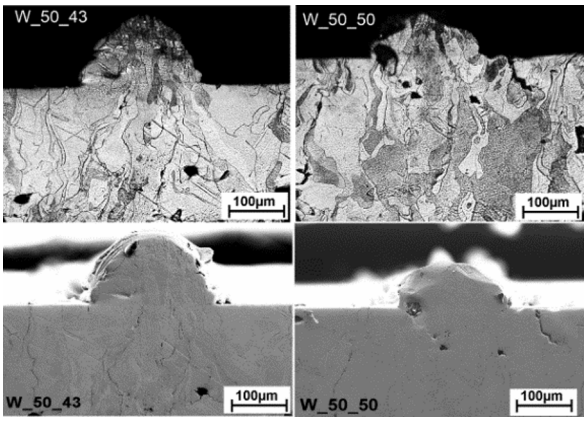

Fig. 7. SEM's showing melt pool cross sections for 50 mm/s scans, 43 µm beam diameter (W_50_43) 50 µm (W_50_50) beam diameter.

EBSD was used to analyse the microstructural texture of tungsten cross-sections to obtain details about the epitaxial growth at melt pool and substrate interface. Fig. 7 displays EBSD Inverse Pole Figure coloured maps of the grain orientation for samples fabricated with the 2DED of 93.02 and 80 J/mm^2. The grain alignment within the tungsten melt pool was influenced by the texture from the substrate. Elongated narrow and directional grains formed vertically, which is typical in LPBF and other AM processes. During LPBF, the previously deposited layer re-melts, allowing solidification by ongoing growth of previously formed grains, which is common in pure metals processing. This solidification texture and narrow structure of grains leads to mechanical properties differing with direction [15, 16]. The pole figures in Fig. 8 (b) reveal comparable textures which are characterised by a large number of

grains aligning with the <100> orientation of the Z axis of the sample. Preferential growth in BCC metals such as tungsten is typically in the <100> growth direction.

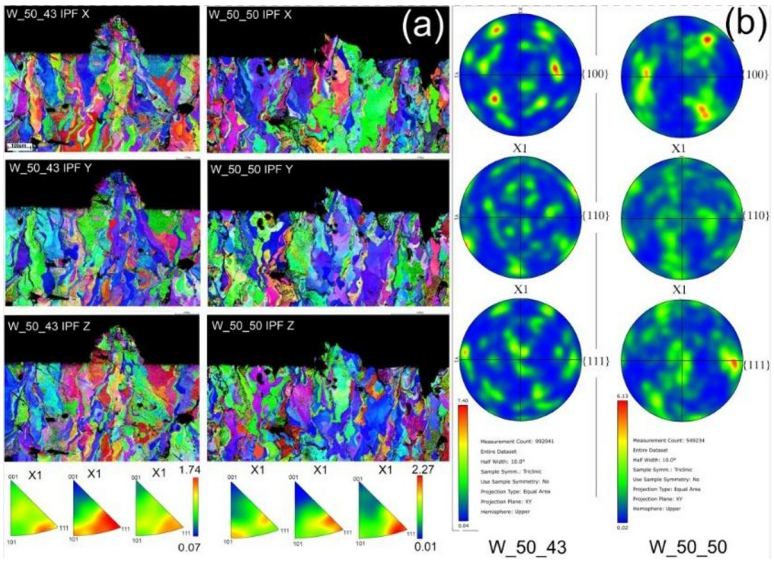

Fig. 8: EBSD Inverse Pole Figure coloured maps of the grain orientation of W_50_43 and W_50_50 melt pool regions shown in x-z build direction views for both substrate and melt pool. Pole figures depicting the tungsten LPBF textures.

Table 3: Details of the parameters used during LPBF, experimentally measured track width results and simulated melt pool analysis results.

Scan (Laser Power =200W)	Scan Speed (mm/s)	Spot Size (µm)	2DED (J/mm^2)	Experimental Track Width (µm)	Simulated Track Width (µm)	αLiquid (Av.)	αSolid (Av.)	Temp [K] (Av.)
W_50_43	50	43	93.02	208 ± 12	166.77	0.7910	0.2582	3237
W_138_43	138	43	33.7	158 ± 5	138.46	0.6645	0.3355	2985
W_225_43	225	43	20.67	124 ± 33	113.26	0.5635	0.4044	2668
W_313_43	313	43	14.86	121 ± 10	97.58	0.4852	0.4665	2475
W_400_43	400	43	11.63	86 ± 11	88.15	0.4626	0.5230	2251
W_50_50	50	50	80	188 ± 11	201.35	0.7300	0.2345	3326
W_138_50	138	50	28.99	136 ± 7	154.19	0.6581	0.3419	3116
W_225_50	225	50	17.78	106 ± 20	125.84	0.5511	0.4265	2863
W_313_50	313	50	12.78	107 ± 4	116.45	0.4828	0.4864	2612
W_400_50	400	50	10	89 ± 15	85	0.3904	0.5550	2389

The results of the single layer tungsten melt tracks, and their dimensions are further presented in Table 3 alongside the corresponding 2D laser energy density values. Table 3 quantifies the melted track width, which ranges from 86 µm to 208 µm. In Fig. 6 the optimised laser beam increased the attainable peak 2-dimensional laser energy density and this is expected, and the resultant melt track width was at the highest at the slowest scan speed of 50 mm/s. At the faster scan speed of 400 mm/s, the melt track width obtained with the 43 µm spot size was unexpectedly less than that with a 50 µm beam diameter. This can be attributed to the minimal difference in 2D linear laser energy densities at the higher scan

speed. The melt pools formed at 400 mm/s have lower values of width as shown in Table 3 which has been reported to be because of the tendency to shape toward a minimum energy state at higher scanning speeds [14].

3.2 Melt pool calculations

In Table 3 the results of the simulated average tungsten melt pool volume fraction (αLiquid), average solid volume fraction (αSolid), track width and average temperature are listed alongside the experimental track width. The melt pool and solid volume fractions were measured along the scan line as indicated in Fig. 5. The simulated track width, αLiquid, αSolid and temperature values of tungsten varied with different scan parameters as expected. The simulated track widths show a consistent trend of increasing with the 2DED but at the laser spot size of 43 µm, the simulated melt widths were narrower than the experimental widths. At the 50 µm laser spot size, the simulated melt widths were consistently wider. However, the central values of the melt pool volume fraction (αLiquid) ranged from 0.3904 to 0.7455 and the smaller laser beam diameter resulted in higher values of the melt pool volume fraction in comparison to the 50 µm diameter beam.

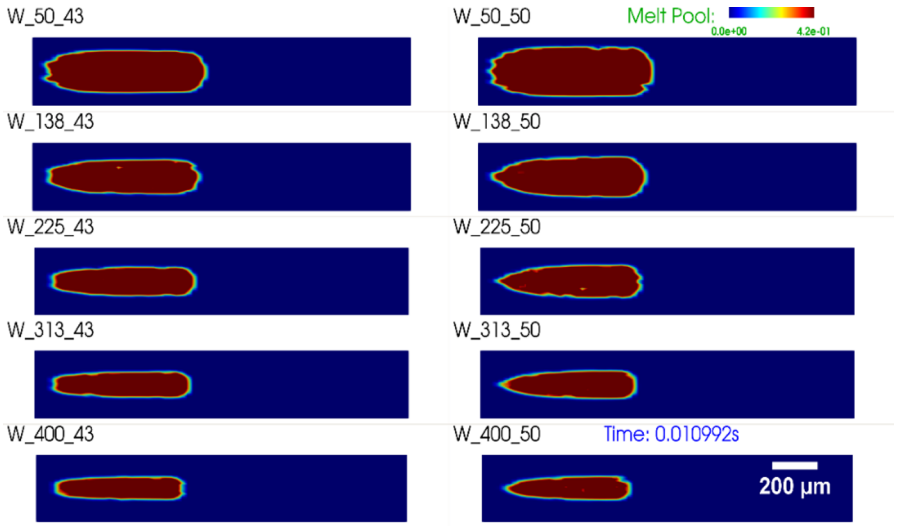

Fig. 9: Melt pool (liquid volume fraction) dynamics after 0.010992 seconds along the scan length during the simulation.

The melt pools were found to be stable during the simulations and this is confirmed by Fig. 9. Fig. 9 shows melt pool dynamics after 0.010992 seconds for the ten-laser beam diameter and scanning speed configurations. The results of the simulated track width were obtained from Fig. 9. The results of the plots of the tungsten solid volume fraction and melt volume fraction along the scan length during the simulations are shown in Fig. 10. Fig. 10 provides more insight into the melting and solidification behaviour of tungsten during the melting. In Fig. 10 the tungsten melt pool volume fraction (black dashed line) represents the proportion of the tungsten material that is in the molten state along longitudinal scan length. The melt volume fraction increased when the laser was active. The solid volume fraction (solid red line) represents the proportion of the tungsten that was in the solid state. The gradients, variations and fluctuations in the melt pool lines at all scan speeds indicate the solidification behaviour of tungsten and how cracks and pores may occur during the LPBF process. Understanding these patterns is crucial for optimising process parameters to achieve

desired material properties and minimise the defects. There are discernible differences in the simulated solid volume fraction between the different scan strategies in the plots in Fig. 10 where the changes in the laser energy density can be seen to affect the solid volume fraction, i.e. the least solid fraction was attained at higher 2DED energy levels (W_50_43 and W_50_50).

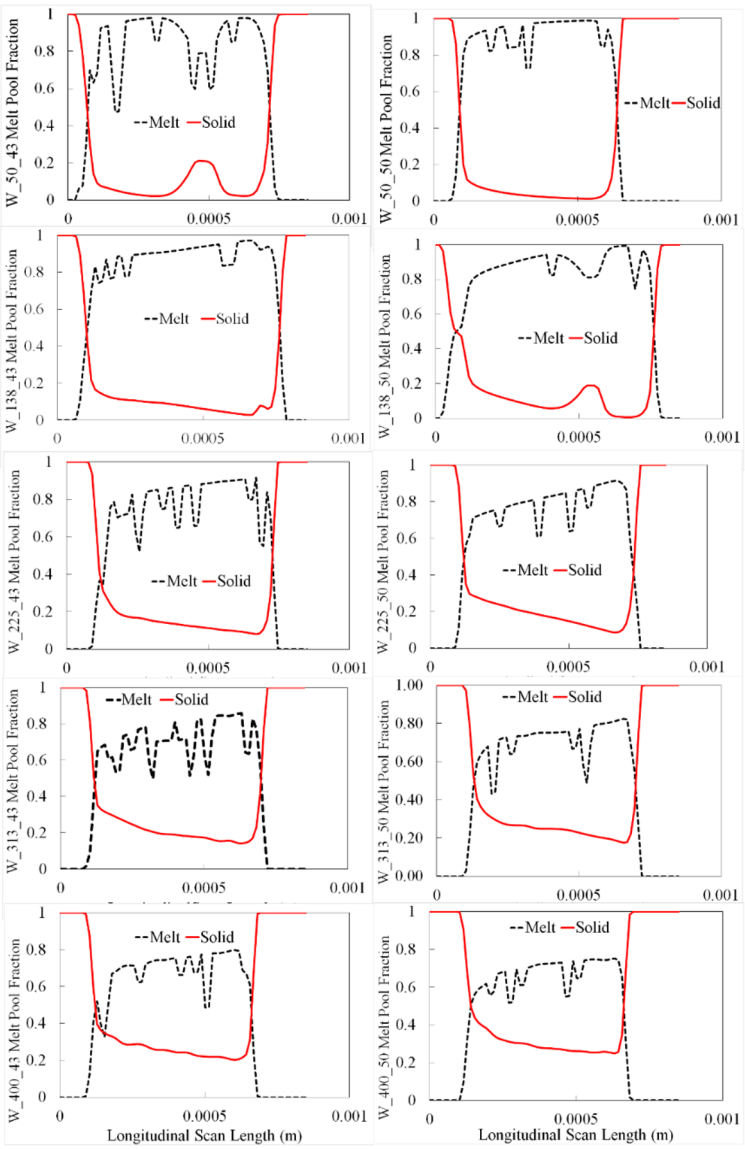

Fig. 10: Plots of the tungsten solid volume fraction (red line) and melt volume fraction (black dashed line) along the scan length during the simulations.

Fig. 11 shows the comparison and correlation of the simulated melt pool volume fraction (αLiquid) and experimental track width. Fig. 11 (a) confirms that the experimental results agree with simulated results, as demonstrated by the correlation coefficient of 0.988. The plots of the temperature evolution along the scan length and measured and the end of laser scanning are shown in Fig. 11 (b). The results not only confirm the average temperature

trends shown in Table 3 and how the larger energy densities yielded higher temperature trends. Fig. 11 (b) also shows that all the scans led to temperatures which peaked between 3826 and 3904K, which is above the melting point of tungsten. The steep cooling profiles indicate the loss of heat which in these simulations can be attributed to convection. The peak temperatures did not exceed the vaporisation temperature of tungsten which is 5823K.

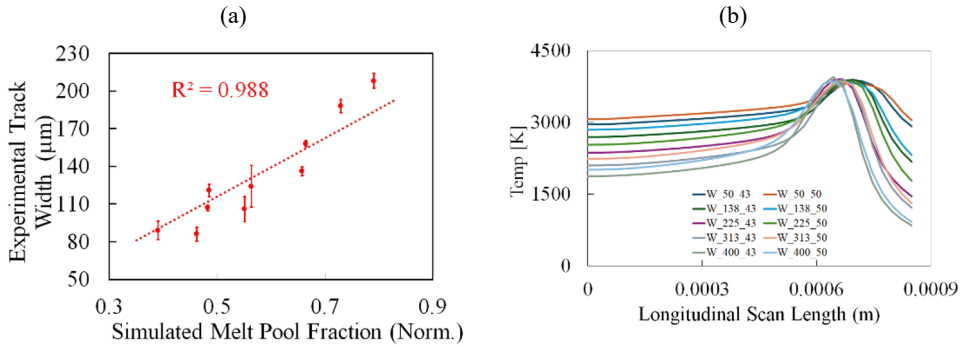

Fig. 11: Comparison and correlation of simulated melt volume fraction and experimental track width (a). Plots of the temperature evolution along the scan length during simulations.

3.3 Simulating defect and pore formation

It was observed in Fig. 10 that the gradients, variations and fluctuations occurred in the melt pool trend lines indicative of breaks in melt pool, particularly during the solidification of tungsten. This gives an insight into how cracks and pores may form during tungsten LPBF. High thermal stresses, and defects such as cracking and porosity are challenges that need to be overcome in tungsten. Fig. 12 shows details of the melt pool evolution of the W_50_43 and W_50_50 simulation results. The colour gradients highlight strong thermal gradients, with solid regions in blue and molten regions transitioning through green to red. The result shown in Fig. 12 show how our approach in this study can be used to assess and mitigate defects formed when melting pure tungsten using LPBF.

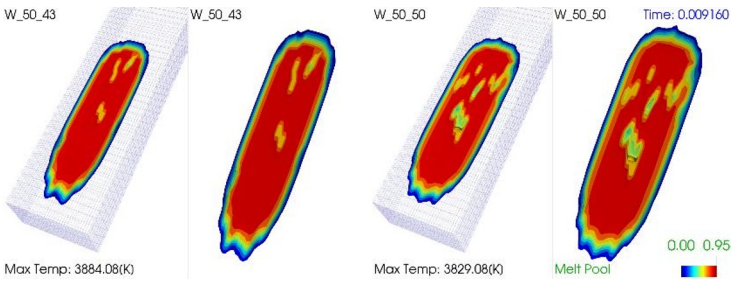

Fig. 12: Details of the melt pool evolution of the W_50_43 and W_50_50 simulation results.

3.3.1 Marangoni effect

In the experimental and simulation results obtained in this study, the correlation of the 2D linear energy density, melt track and melt pool volume fraction is indicative melt flow dynamics similar to the Marangoni effect. The Marangoni effect refers to the movement of mass in the direction of the interface driven by variations in the surface tension, with flow from hot centre to cold boundary in a melt pool. When the surface tension gradient is negative, the result is wider melt pools with reduced depth. If surface tension coefficient is positive, flow direction reverses, resulting in narrower, deeper melt pools. To accurately

replicate experimental observations, it is crucial to include the Marangoni effect in simulations [20]. In this study, Marangoni flow is considered to be significant within the molten metal, particularly where temperature gradients exist. Whilst the *icoReactingMultiphaseInterFoam* is useful for simulating processes such as LPBF, this solver has been reported to have limitations in that it omits the Marangoni effect, a vital heat transfer mechanism within a melt pool. This effect, when coupled with recoil pressure, impacts the shape of the melt pool, causing denudation, spattering, and pore formation [9]. Neglecting the Marangoni effect in LPBF simulations leads to an incomplete understanding of melt pool behaviour. In our model, the impact that the absence of the Marangoni effect may be mitigated by the approach where the recoil pressure, spatter and shielding gas effects have been neglected. Since LPBF relies on precise thermal-fluid control, excluding the Marangoni effect reduces simulation fidelity and limits process optimisation.

In simulations, the Marangoni effect is usually modelled as a tangential surface force along the relevant interface. In order to assess how the *icoReactingMultiphaseInterFoam* solver implements the surface tension, we examined the phase systems components of the software, namely the file *phaseSystem.C* of OpenFOAM version 1912. Whilst the solver does not explicitly implement the Marangoni effect, it includes components to support surface tension modelling. The solver has functions which initialise surface tension models and activates the modelling of interfacial surface tension forces [21]:

$$\overrightarrow{f_\sigma} = \sigma\kappa\vec{n} \tag{10}$$

Where $\overrightarrow{f_\sigma}$ represents the resulting force acting along the liquid surface (added to the momentum equations), σ represents the coefficient of that force, κ represents the geometrical shape of the liquid surface and $\vec{n}$ represents the vector normal to the surface. The equation computes a normal surface tension force but does not include a tangential component that would arise from surface tension gradient. The code and solver would need to have a code for explicitly computing the gradient of surface tension:

$$f_{marangoni} = \nabla_S\sigma(T) = \left(\frac{d\sigma}{dT}\right)\nabla_S T \tag{11}$$

Where $\nabla_S T$ is the surface tension gradient (tangential to the interface) and $\left(\frac{d\sigma}{dT}\right)$ represents surface tension evolution with temperature, which is usually negative. For the implementation to be extended to include the Marangoni effect, which occurs due to changes in surface tension as a result of variations in temperature or concentration, the additional tangential force is given by:

$$\overrightarrow{f_\sigma} = \sigma\kappa\vec{n} + \nabla_S\sigma(T) \tag{12}$$

The *icoReactingMultiphaseInterFoam* solver employs the VOF approach to resolve states of matter. In this case, it calculated the volume fraction αLiquid and αSolid of the phase within a mesh cell. In doing so the solver has not had the capability to track the phase interfaces. In theory, there has been no distinct boundary for applying forces due to forces acting along the interface, which must instead be distributed over the interface thickness by converting surface forces into volume forces. The equations necessary are derived by decomposing the surface tension force, incorporating interface normal vector n, interface curvature κ, surface tension σ and densities of each phase at the interface [21]. Incorporation of the Marangoni effect, recoil pressure and effect of shielding gas will comprise the next stages of this research.

Despite the shortcomings of the *icoReactingMultiphaseInterFoam* solver outlined above, the simulation results in this study yielded good results. To identify and investigate further the simulation results, with the intention of identifying where predictions of melt pool dimensions and thermal gradients may have become less accurate, comparisons were made of the simulated melt pool depth and the surrounding temperature effect. Fig. 13 shows cross sectional analysis of the melt pool (W_50_50) depth alongside the peak temperature. The melt pool shape provides insights into the heat penetration and tungsten behaviour during the simulation. The melt pool depth and formation are shown to be shallow but consistent.

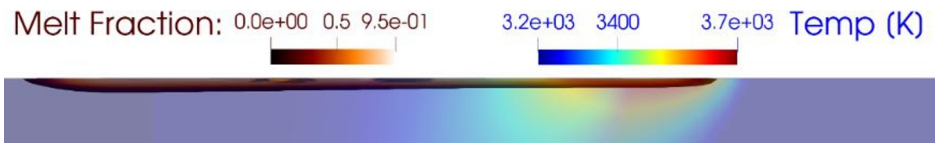

Fig. 13: Cross sectional analysis of the melt pool (W_50_50) incorporating melt pool volume fraction and the thermal gradient acting upon the melt pool.

By comparing simulated track to the experimental melt track width and also comparing the melt volume fraction measured from an extracted contour of the heat affected zone using Paraview, further insights are provided about the correlation between the simulated and the experimental results. With an R^2 value of 0.981, the simulated track width explains approximately 98% of the variance in the experimental results, suggesting a reasonably accurate model. The variance of the simulated melt volume fraction from the HAZ indicates a correlation of 0.958. It can be concluded therefore that the shortcomings of the *icoReactingMultiphaseInterFoam solver* have not been detrimental to this study.

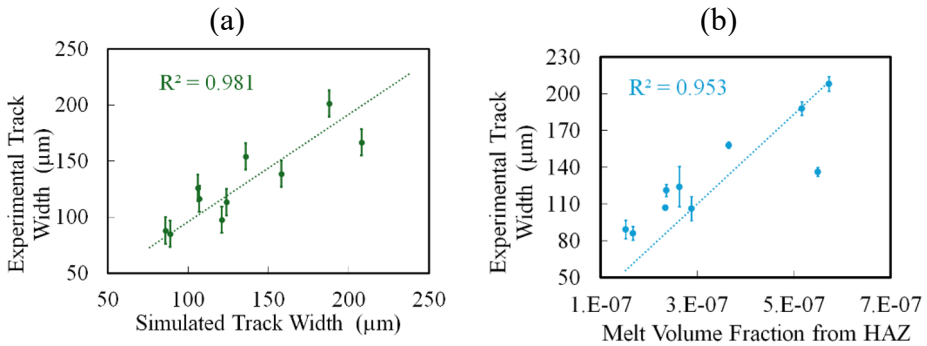

Fig. 14: Further comparisons of the experimental melt pool width with (a) the simulated track width and (b) the melt volume from HAZ.

4 Conclusion

This study demonstrated the significant influence of processing parameters on melt pool behaviour during pure tungsten LPBF. Through a combination of single-track experiments and numerical simulations using OpenFOAM™, it was shown that varying laser focus, and scanning speeds directly affected melt pool morphology, including track width and melt pool volume fraction. The experiments confirmed that the selected parameters were sufficient to achieve full melting and strong bonding with the tungsten substrate. Furthermore, the numerical model was successfully validated against experimental results, reinforcing its reliability for predicting melt pool characteristics in LPBF of tungsten, despite the omission

of the Marangoni effect. These findings contribute valuable insights for optimising process parameters to improve the quality and consistency of tungsten-based additive manufacturing.

The authors would like to thank Dr Matthew Bilton of the University of Liverpool's SEM Shared Research Facility for assistance with EBSD data acquisition.

References

1. A.T. Sidambe, Biocompatibility of Advanced Manufactured Titanium Implants - A Review, Materials, **7**, 12 (2014). https://doi.org/10.3390/ma7128168.
2. A.T. Sidambe, Y. Tian, P.B. Prangnell, P. Fox, Effect of processing parameters on the densification, microstructure and crystallographic texture during the laser powder bed fusion of pure tungsten, Int. J. Refract. Met. Hard. Mater., **78**, (2018). https://doi.org/10.1016/j.ijrmhm.2018.10.004.
3. X. Zhou, X.H. Liu, D.D. Zhang, Z.J. Shen, W. Liu, Balling phenomena in selective laser melted tungsten, J. Mater. Process. Tech., **222**, (2015). https://doi.org/10.1016/j.jmatprotec.2015.02.032.
4. J. Braun, L. Kaserer, J. Stajkovic, K.H. Leitz, B. Tabernig, P. Singer, et al., Molybdenum and tungsten manufactured by selective laser melting - Analysis of defect structure and solidification mechanisms, Int. J. Refract. Met. Hard. Mater., (2019). https://doi.org/10.1016/j.ijrmhm.2019.104999.
5. S. Sharma, K.V.M. Krishna, S.S. Joshi, M. Radhakrishnan, S. Palaniappan, S. Dussa, et al., Laser based additive manufacturing of tungsten: Multi-scale thermo-kinetic and thermo-mechanical computational model and experiments, Acta Mater., **259**, (2023). https://doi.org/10.1016/j.actamat.2023.119244.
6. B. Vrancken, R.K. Ganeriwala, M.J. Matthews, Analysis of laser-induced microcracking in tungsten under additive manufacturing conditions: Experiment and simulation, Acta Mater., **194**, (2020). https://doi.org/10.1016/j.actamat.2020.04.060.
7. A. Sidambe, P. Fox, Melt pool analysis of laser powder bed fusion tungsten - Experimental and simulation, in Proceedings of the Plansee Seminar 2022 Reutte, Austria, (2022).
8. OpenFOAM, OpenFOAM User Guide,(2022). https://www.openfoam.com/documentation/user-guide/1-introduction. (Accessed 25 June 2025).
9. F. Wirth, T. Tonn, M. Schöberl, S. Hermann, H. Birkhofer, V. Ploshikhin, Implementation of the Marangoni effect in an open-source software environment and the influence of surface tension modeling in the mushy region in laser powder bed fusion (LPBF), Model. Simul. Mater. Sci. Eng., **30**, 3 (2022). https://doi.org/10.1088/1361-651X/ac4a26.
10. T. Holzmann, Open Source LASER Boundary Condition with Linear and Circular Spot Motion and Additional Heat-Transfer, in Proceedings of the OpenFOAM User Meeting PFAU XIII (2016).
11. B. Vrancken, R.K. Ganeriwala, A.A. Martin, M.J. Matthews, Microcrack mitigation during laser scanning of tungsten via preheating and alloying strategies, Addit. Manuf., **46**, (2021). https://doi.org/10.1016/j.addma.2021.102158.
12. B. Brown, Characterization of 304L stainless steel by means of minimum input energy on the selective laser melting platform, Masters Thesis, Missouri University Of Science and Technology, Missouri, USA, (2014).
13. J. Lundkvist, CFD Simulation of Fluid Flow During Laser Metal Wire Deposition using OpenFOAM: 3D printing, Masters Thesis, Luleå University of Technology,, Sweden, (2019).

14. R.S. Burdon, Surface tension and the spreading of liquids, (Cambridge University Press, Cambridge, England, 2014).
15. L. Thijs, M.L. Montero Sistiaga, R. Wauthle, Q. Xie, J.-P. Kruth, J. Van Humbeeck, Strong morphological and crystallographic texture and resulting yield strength anisotropy in selective laser melted tantalum, Acta Mater., **61**, 12 (2013). https://doi.org/10.1016/j.actamat.2013.04.036.
16. W. Shifeng, L. Shuai, W. Qingsong, C. Yan, Z. Sheng, S. Yusheng, Effect of molten pool boundaries on the mechanical properties of selective laser melting parts, J. Mater. Process. Technol., **214**, 11 (2014). https://doi.org/10.1016/j.jmatprotec.2014.06.002.
17. L. Erik, S. Wolf-Dieter, Tungsten: properties, chemistry, technology of the element, alloys, and chemical compounds, (Plenum Publishers, New York, USA, 1999).
18. P.-F. Paradis, T. Ishikawa, S. Yoda, Viscosity of liquid undercooled tungsten, J. Appl. Phys., **97**, 10 (2005). https://doi.org/10.1063/1.1896432.
19. C. Tan, K. Zhou, W. Ma, B. Attard, P. Zhang, T. Kuang, Selective laser melting of high-performance pure tungsten: parameter design, densification behavior and mechanical properties, Sci. Technol. Adv. Mater., (2018). https://doi.org/10.1080/14686996.2018.1455154.
20. S.A. Khairallah, A.T. Anderson, A. Rubenchik, W.E. King, Laser powder-bed fusion additive manufacturing: Physics of complex melt flow and formation mechanisms of pores, spatter, and denudation zones, Acta Mater., **108**, (2016). https://doi.org/10.1016/j.actamat.2016.02.014.
21. J.U. Brackbill, D.B. Kothe, C. Zemach, A continuum method for modeling surface tension, J. Comput. Phys., **100**, 2 (1992). https://doi.org/10.1016/0021-9991(92)90240-Y.